



HAL
open science

Modeling Rotational Disruption of Grains and Microwave Emission from Spinning Dust in AGB Envelopes

Ngoc Tram Le, Thiem Hoang, Archana Soam, Pierre Lesaffre, William T.
Reach

► **To cite this version:**

Ngoc Tram Le, Thiem Hoang, Archana Soam, Pierre Lesaffre, William T. Reach. Modeling Rotational Disruption of Grains and Microwave Emission from Spinning Dust in AGB Envelopes. *The Astrophysical Journal*, 2020, 893 (2), pp.138. 10.3847/1538-4357/ab7b5e . hal-02611690

HAL Id: hal-02611690

<https://hal.sorbonne-universite.fr/hal-02611690>


Submitted on 18 May 2020

HAL is a multi-disciplinary open access archive for the deposit and dissemination of scientific research documents, whether they are published or not. The documents may come from teaching and research institutions in France or abroad, or from public or private research centers.

L'archive ouverte pluridisciplinaire **HAL**, est destinée au dépôt et à la diffusion de documents scientifiques de niveau recherche, publiés ou non, émanant des établissements d'enseignement et de recherche français ou étrangers, des laboratoires publics ou privés.



Modeling Rotational Disruption of Grains and Microwave Emission from Spinning Dust in AGB Envelopes

Le Ngoc Tram^{1,2} , Thiem Hoang^{3,4} , Archana Soam¹ , Pierre Lesaffre^{5,6}, and William T. Reach¹ ¹ Stratospheric Observatory for Infrared Astronomy, Universities Space Research Association, NASA Ames Research Center, MS 232-11, Moffett Field, 94035 CA, USA; ngoctram.le@nasa.gov² University of Science and Technology of Hanoi, VAST, 18 Hoang Quoc Viet, Vietnam³ Korea Astronomy and Space Science Institute, Daejeon 34055, Republic of Korea⁴ Korea University of Science and Technology, 217 Gajeong-ro, Yuseong-gu, Daejeon, 34113, Republic of Korea⁵ Laboratoire de Physique de l'École normale supérieure, ENS, Université PSL, CNRS, Sorbonne Université, Université de Paris, France⁶ Observatoire de Paris, PSL University, Sorbonne Université, LERMA, F-75014, Paris, France

Received 2019 July 24; revised 2020 February 10; accepted 2020 February 27; published 2020 April 23

Abstract

Radio observations of some asymptotic giant branch (AGB) star envelopes show excess emission at frequencies below 100 GHz that cannot be explained by thermal dust emission (hereafter anomalous microwave emission (AME)). Moreover, AGB envelopes are a common place where gas molecules condense to form nanoparticles (e.g., polycyclic aromatic hydrocarbons) and large grains. In this paper, we study whether electric dipole emission from rapidly spinning nanoparticles can reproduce the AME observed toward AGB stars. To properly model the size distribution of nanoparticles in the AGB envelope, we take into account both the increase of nanoparticles due to rotational disruption of large grains spun up by radiative torques and the decrease of the smallest nanoparticles due to rotational disruption driven by stochastic gas collisions. We then perform detailed modeling of microwave emission from rapidly spinning nanoparticles from both C-rich and O-rich AGB envelopes using the grain-size distribution constrained by rotational disruption. We find that spinning dust emission is dominant over thermal dust emission at frequencies below 100 GHz. We attempt to fit the observational data of AME using our spinning dust model and demonstrate that spinning dust can reproduce the observed AME in six AGB stars. Finally, we discuss how microwave emission from spinning dust in AGB envelopes could be observed with high-resolution upcoming radio telescopes such the Next Generation Very Large Array and Atacama Large Millimeter/submillimeter Array Band 1. This would be a major leap for understanding AGB envelopes' formation, evolution, and internal structures of dust. Observations would help to distinguish the carrier of AME via comparisons of C-rich and O-rich stars, because polycyclic aromatic hydrocarbons (PAHs) are formed in C-rich AGB stars, while silicates are formed in O-rich stars.

Unified Astronomy Thesaurus concepts: [Circumstellar envelopes \(237\)](#); [Interstellar dust extinction \(837\)](#); [Asymptotic giant branch stars \(2100\)](#); [Radio continuum emission \(1340\)](#); [Interstellar extinction \(841\)](#)

1. Introduction

Late in their evolution, low- and intermediate-mass stars ($1\text{--}8 M_{\odot}$) reach the asymptotic giant branch (AGB) phase, before they become white dwarfs. During this phase, AGB stars lose most of their material (Lamers & Cassinelli 1999) because radiation pressure accelerates them to speeds above their escape velocity. Mass-loss builds an expanding circumstellar envelope (CSE) around the star, containing dust and gas (e.g., Olofsson et al. 2010; Ramstedt et al. 2011; Cox et al. 2012). CSEs of AGB stars can be considered the most significant chemical laboratories in the universe because their effective temperatures are usually low ($T_{\star} \simeq 2000\text{--}3500\text{ K}$), and the mass-loss timescale is long, so molecules can form in the envelope through chemical and physical processes (e.g., Cernicharo et al. 2000; Tenenbaum et al. 2010).

It is well-known that in AGB envelopes, simple molecules condense to form complex molecules, then tiny nanoparticles such as polycyclic aromatic hydrocarbons (PAHs), and tinier submicron-sized grains, before being expelled into the

interstellar medium (ISM) due to radiation pressure. There have been many theoretical studies on the formation of PAHs in the evolved star envelope studied (see Cherchneff 2011 and references therein). While observational evidence of dust grains from AGB envelopes is well established thanks to infrared emission from dust grains, observational evidence for the existence of PAHs, which require mid-IR emission features at 3.3, 6.2, 7.7, 8.6, 11.3, and $17\ \mu\text{m}$ (Leger & Puget 1984; Allamandola et al. 1985; Draine & Li 2007; Smith et al. 2007), is not yet available (see Tielens 2008 for a review). The underlying reason for that is during the AGB stage, the star temperature is low, causing a lack UV photons available that can trigger mid-IR emission of PAHs. Prominent PAH features are usually observed at later stages, such as planetary nebula, due to the higher temperatures in the central star. Therefore, in order to achieve a complete understanding of the formation of dust in AGB star envelopes, it is necessary to develop a new way of observing PAHs/nanoparticles in these environments.

Modern astrophysics establishes that rapidly spinning nanoparticles that have permanent electric dipole moment (e.g., PAHs, nanosilicates, nanoiron particles) can emit electric dipole radiation at microwave frequencies below 100 GHz (Draine & Lazarian 1998; Hoang et al. 2010; Hoang et al. 2016; Hoang & Lazarian 2016). The rotational excitation of

nanoparticles can be achieved in the absence of UV photons, such that microwave emission from spinning dust can be efficient in environments without UV photons like AGB envelopes and dense shocked regions (Hoang & Tram 2019; Tram & Hoang 2019). Therefore, microwave emission could be a unique way for us to probe nanoparticles in the envelopes of AGB stars. In particular, with upcoming advanced radio telescopes, e.g., Atacama Large Millimeter/submillimeter Array (ALMA) Band 1, the Square Kilometer Array, and Next Generation Very Large Array (ngVLA), the potential to observe nanoparticles via spinning dust emission is very promising, and could allow us to have a better understanding of their formation and evolution in general.

Interestingly, previous radio observations show that anomalous microwave emission (AME) at frequencies below 100 GHz from the CSEs around some AGB stars cannot be explained by thermal dust emission, as seen for objects such as IRC +10216 (Sahai et al. 1989 and Menten et al. 2006); or VY CMa, IRc +10216, CIT 6, and R Leo (Knapp et al. 1995); or α Her, IRC +10216, IRC +20370, WX Psc, α Sco, and V Hya (Dehaes et al. 2007). To date, the origin of such excess is not well understood. Therefore, the goal of this paper is to perform detailed modeling of spinning dust emission from nanoparticles in AGB stars and explore whether a spinning dust mechanism can explain such an AME.

To model the emission from spinning dust, we consider the radiation-driven wind model, which starts from a dust-formation zone (i.e., $\sim 5\text{--}10 R_*$), where the temperature varies from 1000 K down to 600 K and the total number density varies from 10^{10} to 10^8 cm^{-3} . Furthermore, dust grains are classified by their spectral features and they correspond to special kinds of envelope properties. Silicates, identified at 9.7 and 18 μm , are considered a major feature of oxygen-rich stars ($C/O < 1$) (Kwok 2004). In contrast, in carbon-rich stars ($C/O > 1$), one expects to observe prominent mid-IR features from PAHs. In this paper, we will model the microwave emission from spinning PAHs for a typical representative of carbon-rich AGB stars (IRC +10216) and from nanosilicates for a typical representative of oxygen-rich AGB stars (IK Tau).

Owing to their large sizes, AGB stars are among the most luminous objects in the sky, with luminosities of order $10^4 L_\odot$. Thus, the radiation field in their CSEs is remarkably strong. Recently, Hoang et al. (2019) showed that a strong radiation field can torque large dust grains up to $\sim 10^9$ revolutions per second, a rate at which the centrifugal force can disrupt a large grain into smaller ones. In addition, Hoang & Tram (2019) and Tram & Hoang (2019) showed that very small grains (referred to as nanoparticles whose sizes are lower than 10 nm) can be spun up to suprathreshold rotation by stochastic torques induced by gas bombardment in a dense and hot medium. As a result, smallest nanoparticles are disrupted into smaller tiny fragments when the centrifugal force exceeds the material strength, after which dust particles are thermally sublimated into the gas phase (Guhathakurta & Draine 1989). These two disruption mechanisms are then taken into account in our model because they can modify the size distribution of dust grains in AGB envelopes.

The structure of this paper is as follows. Section 2 describes the parametric physical model of AGB envelopes. We constrain the upper limit of grain sizes with the radiative torque disruption (RATD) mechanism in Section 3, and the lower limit of the size of nanoparticles due to mechanical torques in Section 4. In Section 5, we review the spinning dust

model, and calculate the spectral energy distribution (SED) from spinning dust for two examples of AGB stars. An extended discussion of the implications of our results for explaining AME in AGB envelopes occurs in Section 6. A summary of our main results is presented in Section 7.

2. Physical Model of AGB Envelopes

During the AGB phase, a star loses most of its mass through stellar winds. Very close to the central star, where it is too hot for dust grains to form, the ejection mechanism is not yet well unified. The pulsation process is believed to accelerate gas above the escape velocity, sending it radially outward (e.g., Hoefner & Dorfi 1997; Willson 2000; and see Tram et al. 2018 for review). Farther from the star, where the gas temperature decreases to the condensation temperatures, dust grains form. Subsequently, dust grains are accelerated by radiation pressure and transfer their momentum to gas molecules through collisions. Collisions result in a drag force (Gilman 1972) that allows gas beyond the dust-formation distance to overcome the gravitational well of the star. The resulting winds are called dust-driven or radiation-driven winds. Here we briefly describe our parametric physical model of AGB envelopes for a radiation-driven wind, which will be used as the framework for calculating rotational disruption of dust grains and spinning dust emission.

2.1. Gas-density Profile

Let \dot{M} be the rate of mass loss of an AGB star, and we assume a spherical envelope. The gas density at distance r is then given by

$$\begin{aligned} n_{\text{gas}}(r) &= \frac{\dot{M}}{4\pi r^2 m_{\text{gas}} v_{\text{exp}}} \\ &= 10^6 \left(\frac{\dot{M}}{10^{-5} M_\odot} \right) \left(\frac{10^{15} \text{ cm}}{r} \right)^2 \left(\frac{10 \text{ km s}^{-1}}{v_{\text{exp}}} \right) \text{ cm}^{-3}, \end{aligned} \quad (1)$$

where v_{exp} is the expansion velocity of the outflow. The typical mass-loss rates are $\dot{M} \sim 1\text{--}10 \times 10^{-5} M_\odot \text{ yr}^{-1}$. For cold AGB stars, we take $m_{\text{gas}} = 2.33$ amu because hydrogen in the CSEs around these stars is predominantly molecular (Glassgold & Huggins 1983; Tram et al. 2018). For hot AGB stars, on the contrary, the atomic form of hydrogen dominates the CSE, therefore we take $m_{\text{gas}} = 1.3$ amu (90% H and 10% He). The critical temperature to distinguish cold or hot AGB stars depends on the density of the stellar photosphere, e.g., $T_*^{\text{cri}} \simeq 2500$ K for stars with density $\geq 10^{14} \text{ cm}^{-3}$ (Tram et al. 2018). The expansion velocity is likely constant for a radiation-driven wind model, as demonstrated by Tielens (1983) and Krueger et al. (1994).

2.2. Gas Temperatures

In the envelope beginning at the condensation radius (r_c), where the gas expands adiabatically at constant v_{exp} , the radiative heating is dominant because the gas is weakly or no longer shielded by dust so that the temperature drops gradually with the distance, and we approximate its profile as a power law as: (e.g., Mamon et al. 1988; Agúndez & Cernicharo 2006;

Table 1
Circumstellar Envelope Models

Parameters	IRC +10216	IK Tau	References
L_* (L_\odot)	8640	7700	(1); (9)
\dot{M} ($M_\odot \text{ yr}^{-1}$)	2×10^{-5}	4.5×10^{-6}	(2); (10)
T_* (K)	2200	2100	(3); (9), (10)
T_0 (K)	14.6	707	(4); (11)
R_* (cm)	4.5×10^{13}	3.1×10^{13}	(5); (10)
r_c (R_*)	5	8.7	(6); (12)
r_0 (R_*)	1385	5.20	(4); (11)
r_{out} (R_*)	1.32×10^4	2×10^4	(7); (12)
v_{exp} (km s^{-1})	14.5	24	(8); (13)
α_{gas}	0.72 ($r < r_0$)	0.79	(4); (11)
	0.54 ($r \geq r_0$)		(4)
D (pc)	130	265	(5); (9)

References. (1) Menten et al. (2012); (2) Crosas & Menten (1997); (3) Matthews et al. (2015), (4) taken from the fit of Mamon et al. (1988) to Kwan & Linke (1982); (5) Tram et al. (2018); (6) Agúndez & Cernicharo (2006); (7) Sahai & Chronopoulos (2010); (8) Knapp et al. (1998); (9) Maercker et al. (2016); (10) De Beck et al. (2010); (11) fit to Decin et al. (2010); (12) Decin et al. (2010); (13) Justtanont et al. (2012).

Decin et al. 2010; Li et al. 2016):

$$T_{\text{gas}}(r) = T_0 \left(\frac{r}{r_0} \right)^{-\alpha_{\text{gas}}}, \quad (2)$$

where T_0 , r_0 , and α_{gas} are parameters whose values are given in Table 1.

2.3. Grain Temperature

The grain-temperature evolution is determined by the balance between the heating and cooling rates. Grains are heated by collisions with the gas particles and by absorption of stellar or ambient radiation. Grains are cooled by collisional energy transfer and by thermal radiation. A detailed profile of the dust temperature in a realistic envelope can be modeled by solving the radiative transfer equation for a given dust opacity (Winters et al. 1994). But we assume here that the stellar radiation dominates. In a simple case where the grain absorption efficiency can be approximated as a power law of wavelength $Q_{\text{abs}} \sim \lambda^{-s}$, the dust temperature can be derived as (Habing & Olofsson 2003)

$$T_d(r) = T_* \left(\frac{R_*}{2r} \right)^{2/(4+s)}, \quad (3)$$

where T_* and R_* are the temperature and radius of star. Observations suggest $s \simeq 1$.

2.4. Physical Properties of a C-star and an O-star

We apply the parametric models described above to calculate the physical properties of the freely expanding wind in the CSEs around the well-known C-rich AGB stars (namely IRC +10216) and O-rich (namely IK Tau), as illustrated in Figure 1. For IRC +10216, the profile of the gas temperature is taken from Mamon et al. (1988), who fitted the power law to the theoretical results of Kwan & Linke (1982). For IK Tau, we similarly fit the power law to the gas-temperature profile that is derived from observational ^{12}CO lines (Decin et al. 2010). Other parameters are listed in Table 1.

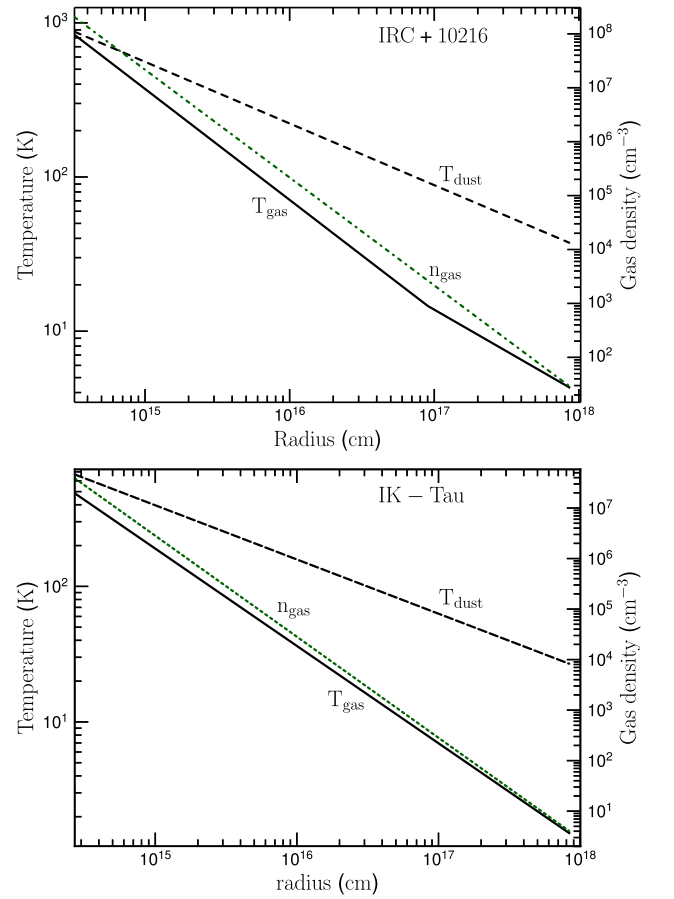


Figure 1. Physical properties of the freely expanding wind in the CSEs around IRC +10216 star (top panel) and IK Tau (bottom panel).

2.5. Drift Velocity for Nanoparticles

Once dust grains have formed, they scatter and absorb stellar photons, leading to a radiative force that pushes them outward away from the star. The radiation force on a grain of radius a at distance r due to the central star is given by

$$F_{\text{rad}} = \frac{L_* \bar{Q}_{\text{rp}} \pi a^2}{4\pi r^2 c}, \quad (4)$$

where c is the speed of light, \bar{Q}_{rp} is the radiation pressure efficiency, \bar{Q}_{rp} is the wavelength-averaged radiation pressure efficiency weighted by the stellar spectrum, and L_* is the total stellar luminosity. Let v_{drift} be the drift velocity of grains through the gas. If the drift speed is much larger than the thermal speed of gas particles, the drag force per unit volume of the gas is $F_{\text{drag}}(a) = \pi a^2 \rho v_{\text{drift}}^2 n_{\text{gas}}$, where a is the radius of a single grain.⁷ On the other hand, if the drift speed is lower than the thermal speed of the gas, the drag force $F_{\text{drag}}(a) = \pi a^2 \rho c_s v_{\text{drift}} n_{\text{gas}}$. To combine those limits, we can express the drag force as follows

$$F_{\text{drag}}(a) = \pi a^2 n_{\text{gas}} \rho v_{\text{drift}} \sqrt{v_{\text{drift}}^2 + c_s^2}. \quad (5)$$

Because the mean free path of the gas is larger than the typical dust radii, and the velocities of gas and dust are different, the grains are not positioned coupled to the gas. Despite the fact

⁷ When the drift velocity is above a percent of the light speed, the drag force decreases with increasing velocity, as discovered by Hoang (2017).

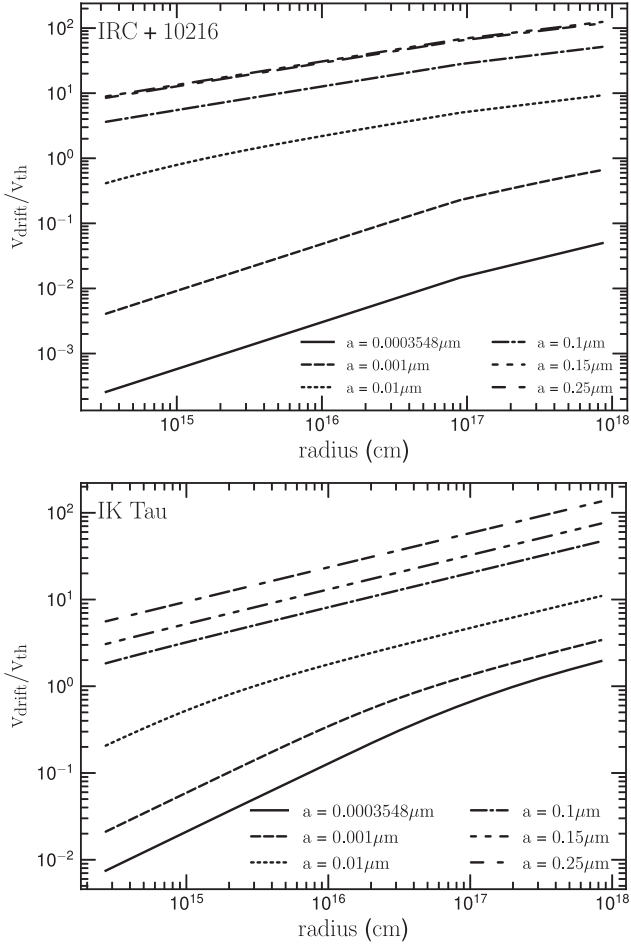


Figure 2. Dimensionless drifting parameters for IRC +10216 star (top panel) and IK Tau (bottom panel) calculated for different grain sizes. Large grains are moving supersonically, but the smallest nanoparticles are moving subthermally.

that the grains collide with only a small fraction of the gas particles, Gilman (1972) indicates that the subsequent collisions among the gas molecules allow the momentum that they receive from the radiation field to be transferred to the gas. Gilman (1972) also demonstrates that the small grains rapidly reach the terminal drift velocity. The grains move at the terminal drift velocity when the radiation force balances the drag force:

$$v_{\text{drift}}^2 = \frac{1}{2} \left[\left[\left(\frac{2v}{\dot{M}c_l} \bar{Q}_{\text{rp}} L_* \right)^2 + c_s^4 \right]^{0.5} - c_s^2 \right], \quad (6)$$

where $c_s = (2k_B T_{\text{gas}}/m_{\text{gas}})^{1/2}$ is the sound speed in the gas. We define the dimensionless drifting parameter $s_d = v_{\text{drift}}/c_s$. As a limitation, if the thermal speed is much lower than the outflow speed and the grain size is much lower than the wavelength, $\bar{Q}_{\text{rp}} \propto a$ and therefore $s_d(r) \sim v_{\text{drift}}(r) \propto a^{0.5}$, the drift between gas and big dust grains is larger than that of small dust grains.

In Figure 2, we show the normalized grain-drift velocity $v_{\text{drift}}/v_{\text{th}}$ calculated for different grain sizes. The drift velocity s_d tends to increase with increasing grain distance because the gas temperature decreases. Large grains can be accelerated to

Table 2
Abundance Relative to H_2 of Major Chemical Species in AGB Envelope

IRC +10216		
Species	Abundances	Note
$x(\text{H}_2)$	⁽¹⁾ ≈ 1	
$x(\text{He})$	⁽²⁾ 2×10^{-1}	
$x(\text{CO})$	⁽²⁾ 6×10^{-4}	
$x(\text{C}^+)$	⁽³⁾ 1.5×10^{-5}	$r < 6 \times 10^{17}$ cm
$x(\text{H}^+)$	⁽³⁾ 3.7×10^{-8}	$r \geq 6 \times 10^{17}$ cm
$x(\text{S}^+)$	⁽³⁾ 5×10^{-8}	$r \geq 3 \times 10^{16}$ cm
IK Tau		
Species	Abundances	Note
$x(\text{H}_2)$	⁽¹⁾ ≈ 1	
$x(\text{CO})$	⁽⁴⁾ 10^{-4}	$r < 2.5 \times 10^{17}$ cm
$x(\text{O})$	⁽⁴⁾ 1×10^{-4}	$r \geq 10^{16}$ cm
$x(\text{N})$	⁽⁴⁾ 2.5×10^{-4}	$r \geq 2 \times 10^{17}$ cm
$x(\text{N}_2)$	⁽⁴⁾ 1.8×10^{-4}	$r \leq 6 \times 10^{17}$ cm
$x(\text{C}^+)$	⁽⁴⁾ 2×10^{-4}	
$x(\text{e}^-)$	⁽⁴⁾ 2×10^{-4}	

References. (1) Glassgold & Huggins (1983), Tram et al. (2018); (2) Agúndez & Cernicharo (2006); (3) Millar et al. (2000); (4) Li et al. (2016).

supersonic motion, while the smallest nanoparticles, of size $a \lesssim 1$ nm, are mostly moving at subsonic speeds.

2.6. Ionization

In the AGB and post-AGB stages, the star is relatively cool, with $T_* \sim 2000\text{--}3000$ K. Therefore, its ionizing radiation is negligible, and the gas remains mostly neutral. In the planetary nebula (PN) stage, the star has contracted to a white dwarf with high temperature, and the envelope is ionized. Nanoparticles in the outer envelope will be affected by interstellar UV photons, which also ionize gas atoms. The most abundant species in C-rich and O-rich stars are listed in Table 2 with references.

3. Rotational Disruption of Large Grains by Radiative Torques

3.1. Radiation Field from an AGB Star

In this paper, we are considering the radiative-driven wind, which should start from the dust-condensation zone. Normally, this zone is located quite far from the central star (e.g., $\approx 5R_*$ for the case of IRC +10216). Thus, we can neglect the angle-dependence of a radiation field on dust-grain particles. Therefore, the radiation energy density from an AGB star at a distance r is

$$u_{\text{rad}} \simeq 0.46 \frac{L_4 e^{-\tau}}{r_{\text{au}}^2} \quad (\text{erg cm}^{-3}), \quad (7)$$

where $L_4 = L_*/10^4 L_{\odot}$, and τ is the total optical depth. The averaged interstellar radiation field (ISRF) from other Milky Way stars has an energy density $u_{\text{ISRF}} = 8.64 \times 10^{-13}$ erg cm $^{-3}$ (Mathis et al. 1983). The relative strength of the radiation field from the AGB star is then

$$U \equiv \frac{u_{\text{rad}}}{u_{\text{ISRF}}} \simeq 5.3 \times 10^{11} \frac{L_4 e^{-\tau}}{r_{\text{au}}^2} \quad (8)$$

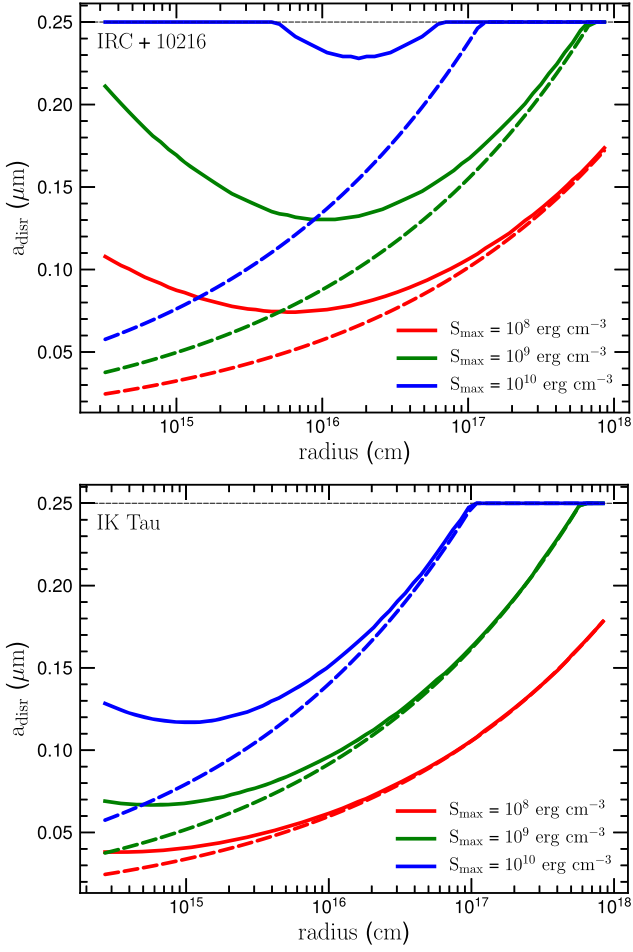


Figure 3. Disruption size of dust grains vs. distance from the star in the CSEs of IRC +10216 (top panel) and IK Tau (bottom panel) for different tensile strengths (S_{\max}). The initial maximum grain size is chosen as $0.25 \mu\text{m}$. The corresponding colored dashed lines are disruption sizes computed by Equation (16). The disruption size is smaller for weaker grain materials (i.e., lower S_{\max}).

For IRC +10216 at $5R_*$, $U \simeq 2 \times 10^9$, whereas at $10^4 R_*$, $U \simeq 3 \times 10^2$ (neglecting extinction).

3.2. Rotational Disruption by Radiative Torques

As revealed in Hoang et al. (2019), a strong radiation field can spin large grains up to a maximum angular velocity

$$\omega_{\text{RAT}} = \frac{\Gamma_{\text{RAT}} \tau_{\text{damp}}}{I}, \quad (9)$$

where I is the grain inertial moment, Γ_{RAT} is the radiative torque (Draine & Weingartner 1996; Lazarian & Hoang 2007; Hoang & Lazarian 2008; Herranen et al. 2019), and τ_{damp} is the total damping timescale.

The averaged radiative torque applied on a grain of irregular shape with *effective* size a is (see Hoang et al. 2019 and references therein)

$$\Gamma_{\text{RAT}} = \pi a^2 \gamma u_{\text{rad}} \frac{\bar{\lambda}}{2\pi} \bar{Q}_{\Gamma}, \quad (10)$$

where γ is the degree of anisotropy of the radiation field ($0 \leq \gamma \leq 1$), $\bar{\lambda}$ is the average wavelength of the radiation field (i.e., $\bar{\lambda} = 2.42 \mu\text{m}$ for IRC +10216 and $\bar{\lambda} = 2.53 \mu\text{m}$ for IK

Tau). Above, the radiative torque efficiency averaged over the radiation spectrum is approximately $\bar{Q}_{\Gamma} \simeq 2(\bar{\lambda}/a)^{-2.7}$ for $a \leq \bar{\lambda}/1.8$, and $\bar{Q}_{\Gamma} \sim 0.4$ for $a > \bar{\lambda}/1.8$. However, we adopt the maximum grain size to be $0.25 \mu\text{m}$, as deduced from observations (Mathis et al. 1977). Therefore, we just consider $a \leq \bar{\lambda}/1.8$ in this work.

The total rotational damping of dust grains consists of collisional damping due to collisions with gas species (Jones & Spitzer 1967) and IR damping due to IR emission, and the characteristic damping time is described by (see Hoang et al. 2019)

$$\tau_{\text{damp}} = \frac{\tau_{\text{gas}}}{1 + F_{\text{IR}}}, \quad (11)$$

where the characteristic timescale of collisional damping is

$$\tau_{\text{gas}} \simeq 8.74 \times 10^4 a_{-5} \hat{\rho} \left(\frac{30 \text{ cm}^{-3}}{n_{\text{H}}} \right) \left(\frac{100\text{K}}{T_{\text{gas}}} \right)^{1/2} \text{ yr}, \quad (12)$$

with $n_{\text{H}} = n(\text{H}) + 2n(\text{H}_2)$ being the proton number density, and the dimensionless IR damping coefficient

$$F_{\text{IR}} \simeq \left(\frac{0.4U^{2/3}}{a_{-5}} \right) \left(\frac{30 \text{ cm}^{-3}}{n_{\text{H}}} \right) \left(\frac{100\text{K}}{T_{\text{gas}}} \right)^{1/2}, \quad (13)$$

where $a_{-5} = a/(10^{-5} \text{ cm})$, and $\hat{\rho} = \rho/(3 \text{ g cm}^{-3})$. Here we have assumed that dust grains are in the thermal equilibrium established by radiative heating of starlight and radiative cooling by IR emission.

Plugging Γ_{RAT} and τ_{damp} into Equation (9) yields the maximum rotation rate spun up by RATs:

$$\omega_{\text{RAT}} \simeq 6.6 \times 10^9 \gamma a_{-5}^{0.7} \bar{\lambda}_{2.42}^{-1.7} \times \left(\frac{U_6}{n_5 T_2^{1/2}} \right) \left(\frac{1}{1 + F_{\text{IR}}} \right) \text{ rad s}^{-1}, \quad (14)$$

with $U_6 = U/10^6$, $n_5 = n_{\text{H}}/10^5 \text{ cm}^{-3}$, $T_2 = T_{\text{gas}}/100 \text{ K}$, and $\bar{\lambda}_{2.42} = \bar{\lambda}/2.42 \mu\text{m}$.

Equation (14) reveals that the rotational rate induced by RATs depends on the term $U/n_{\text{H}} T_{\text{gas}}^{1/2}$ and F_{IR} . Thus, grains at $154R_*$ in the CSE of IRC +10216, where $U = 10^6$, can be spun up to $\omega_{\text{RAT}} \sim 10^9 \text{ rad s}^{-1}$. However, when a grain of size a is rotating at an angular velocity ω , it develops a centrifugal stress due to the centrifugal force, which scales as $S = \rho a^2 \omega^2 / 4$ (Hoang et al. 2019). Then, if the rotation rate increases to a critical limit such that the stress induced by centrifugal force exceeds the tensile strength of the material, grains are disrupted instantaneously. The critical angular velocity for the disruption is given by

$$\frac{\omega_{\text{cri}}}{2\pi} = \frac{1}{\pi a} \left(\frac{S_{\max}}{\rho} \right)^{1/2} \simeq 1.8 \times 10^9 a_{-5}^{-1} \hat{\rho}^{-1/2} S_{\max,10}^{1/2} \text{ Hz}, \quad (15)$$

where S_{\max} is the maximum tensile strength of dust material and $S_{\max,10} = S_{\max}/(10^{10} \text{ erg cm}^{-3})$.⁸

The exact value of S_{\max} depends on the dust-grain composition and structure. Compact grains can have higher

⁸ An equivalent unit for the tensile strength is dyne cm^{-2} ; in this paper we use erg cm^{-3} units for convenience.

S_{\max} than porous grains. Ideal material without impurities, such as diamond, can have $S_{\max} \geq 10^{11}$ erg cm $^{-3}$. Burke & Silk (1974) suggested that $S_{\max} \sim 10^9$ – 10^{10} erg cm $^{-3}$ for polycrystalline bulk solids (see also Draine & Salpeter 1979). Mathis & Whiffen (1989) suggested composite grains would have much lower strength. In Draine & Salpeter (1979), the value $S_{\max} = 5 \times 10^9$ erg cm $^{-3}$ is taken for small graphite grains. In the following, nanoparticles with $S_{\max} \gtrsim 10^{10}$ erg cm $^{-3}$ are referred to as strong materials, and those with $S_{\max} < 10^{10}$ erg cm $^{-3}$ are called weak materials.

For each location in the AGB envelope with given n_{H} , T_{gas} and U , one can obtain the critical grain size of rotational disruption by radiative torques by setting $\omega_{\text{RAT}} \equiv \omega_{\text{cri}}$.

Figure 3 shows the disruption size of dust grains by radiative torques with respect to distance from the C-rich star IRC +10216 and the O-rich star IK Tau, assuming different tensile strengths. Very close to the star, rotational damping by gas collisions is very efficient because $n_{\text{H}} \gg 1$ and $T_{\text{gas}} \gg 1$ and dominates over IR damping (i.e., $F_{\text{IR}} \ll 1$), resulting in a very short damping timescale ($\tau_{\text{damp}} \sim \tau_{\text{gas}} \ll 1$ yr). As a result, grains lose their angular momentum rapidly and cannot be spun up to critical rotation rates, and large grains can survive rotational disruption. Farther away from the star, the rotational damping rate is decreased due to the rapid decrease of n_{H} and T_{gas} with distance r , and large grains can be spun up to extremely fast rotation by radiative torques and are disrupted into small sub-fragments. The disruption size decreases with increasing distance from the star. Finally, when grains are far enough from the star, the collisional damping is subdominant compared to IR damping, i.e., $F_{\text{IR}} \gg 1$ and $U \gg 1$ and the disruption size of grains can be analytically estimated as (Hoang et al. 2019; Hoang 2019)

$$\left(\frac{a_{\text{disr}}}{0.1 \mu\text{m}} \right)^{2.7} \simeq 2.12 \gamma^{-1} \bar{\lambda}_{2.42}^{1.7} \times \left(\frac{U_6}{1.2} \right)^{-1/3} S_{\max,10}^{1/2}, \quad (16)$$

which does not depend on the gas properties, as shown by the dashed lines.

4. Rotational Disruption of Nanoparticles by Stochastic Mechanical Torques

4.1. Rotational Dynamics of Nanoparticles

In dense regions, such as the CSEs of AGB stars, Jones & Spitzer (1967) showed that collisions with gas atoms and molecules rotate dust grains. In addition, nanoparticles are directly bombarded by molecules and atoms (including elements heavier than H), and they experience long-distance interactions with passing ions (Draine & Lazarian 1998; Hoang et al. 2010; Hoang & Tram 2019).

Following Jones & Spitzer (1967) and Hoang & Tram (2019), one can define the dimensionless damping and excitation coefficients for interaction processes with respect to the damping and excitation coefficients of purely hydrogen neutral-grain collisions as

$$\frac{d\langle I\omega_r \rangle}{dt} = \langle \Delta J'_r \rangle_{\text{H}} \times \sum_j F_j, \quad (17)$$

$$\frac{d\langle I\omega^2 \rangle}{dt} = \frac{\langle (\Delta J')^2 \rangle_{\text{H}}}{I} \times G = \frac{3I\omega_T^2}{\tau_{\text{H}}} \times \sum_j G_j, \quad (18)$$

where $\langle \Delta J'_r \rangle$ and $\langle (\Delta J')^2 \rangle$ are the mean decrease of grain angular momentum along the r -axis and the mean increase of

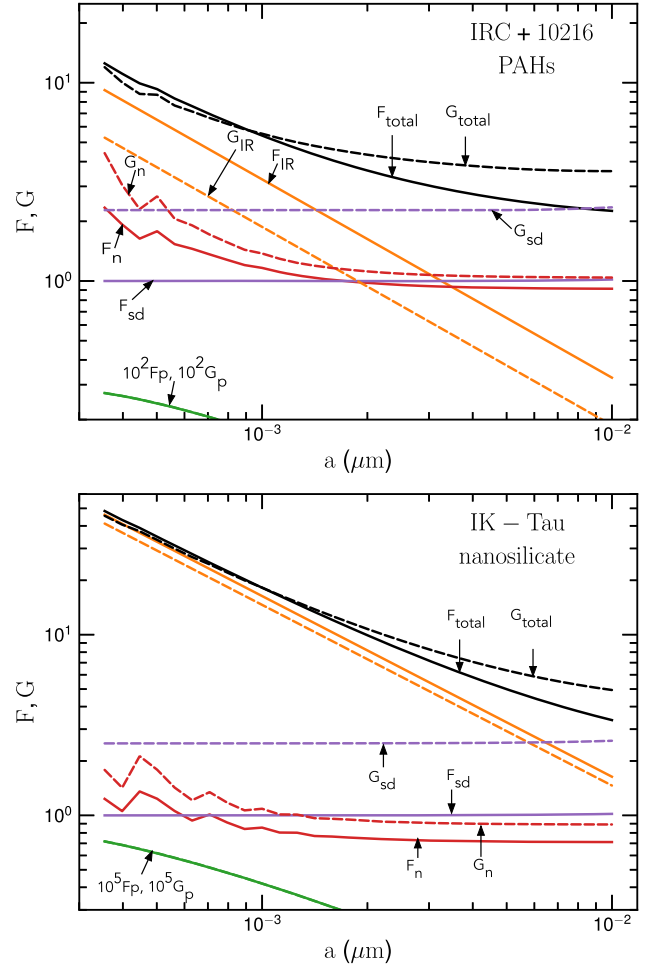


Figure 4. Rotational damping (F , solid lines) and excitation (G , dashed lines) coefficients of various processes computed for PAH and nanosilicates at $10R_*$.

rotational energy per unit time by colliding with pure hydrogen, respectively, and ω_T is the thermal angular momentum of grains at temperature T_{gas} . The dimensionless damping (F) and excitation (G) coefficients are defined, respectively, as

$$F = F_{\text{sd}} + F_{\text{IR}} + F_n + F_p + F_i, \quad (19)$$

$$G = G_{\text{sd}} + G_{\text{IR}} + G_n + G_p + G_i, \quad (20)$$

where suffixes sd, IR, n , p , and i stand for gas-grain drift, infrared, neutral, plasma, and ion, respectively. F_{sd} and G_{sd} are computed as in Roberge et al. (1995; the details are described in Section 3 in Hoang & Tram 2019), whereas other coefficients are computed as described in Sections 4 and 5 in Draine & Lazarian (1998). Note that $F_j = G_j = 1$ for grain collisions with purely atomic hydrogen gas. Figure 4 shows the obtained values of F and G for various processes for PAH and silicates grains. As shown, IR emission is dominant for rotational damping of the smaller grains ($< 0.005 \mu\text{m}$) and gas-grain drift is dominant for larger grains.

Let T_{rot} be the rotational temperature of spinning nanoparticles, such that $I\langle \omega^2 \rangle = 3k_B T_{\text{rot}}$. Thus, using the rms angular velocity from Draine & Lazarian (1998), we obtain

$$\frac{T_{\text{rot}}}{T_{\text{gas}}} = \frac{G}{F} \frac{2}{1 + [1 + (G/F^2)(20\tau_{\text{H}}/3\tau_{\text{ed}})]^{1/2}}, \quad (21)$$

where τ_H and τ_{ed} are the characteristic damping times due to gas collisions and electric dipole emission (see Draine & Lazarian 1998). As $\tau_{ed}/\tau_H \sim (a/3.5 \text{ \AA})^7 (n_H/10^4 \text{ cm}^{-3})$ (see Hoang et al. 2010), this ratio is much bigger than 1 as long as $n_H > 10^5 \text{ cm}^{-3}$. Therefore, $T_{rot}/T_{gas} \sim G/F$, i.e., the rotational temperature is only determined by the rotational damping (F) and excitation (G) coefficients.

Accordingly, the rotation rate at the rotational temperature T_{rot} is given by

$$\begin{aligned} \frac{\omega_{rot}}{2\pi} &= \frac{1}{2\pi} \left(\frac{3k_B T_{rot}}{I} \right)^{1/2} \\ &\simeq 1.4 \times 10^{10} \hat{\rho}^{-1/2} a_{-7}^{-5/2} \left(\frac{T_{rot}}{10^3 \text{ K}} \right)^{1/2} \text{ Hz.} \end{aligned} \quad (22)$$

4.2. Rotational Disruption of Nanoparticles by Stochastic Mechanical Torques

To calculate the smallest size a_{min} that nanoparticles can withstand the rotational disruption, we compute $\langle \omega^2 \rangle$ using the rotational temperature T_{rot} as given by Equation (21) at each radius for a grid of grain sizes from 0.35 to 10 nm and compare it with ω_{cri} .

Figure 5 shows the obtained minimum size a_{min} as a function of radius in CSE for different values of S_{max} and two AGB models. Strong nanoparticles can survive (green line), while weak nanoparticles can be destroyed (blue and orange lines). The disruption size drops gradually with distance from the central star due to the rapid decrease of gas temperature with distance.

5. Spinning Dust Emission

The emission from spinning dust is detailed in Hoang & Tram (2019). In this section, we briefly recall the principles of this model.

5.1. Size Distribution of Nanoparticles Modified by Rotational Disruption

In the case without rotational disruption, we assume that dust grains in AGB envelopes consist of two populations, very small grains (nanoparticles) and larger grains, which we refer to as the *original dust populations*. In the presence of rotational disruption, the smallest nanoparticles are removed by mechanical torques, whereas large grains are disrupted into smaller fragments which comprise nanoparticles, corresponding to the modified dust population. The size distribution of these modified dust populations is unknown, and below we adopt a simplified strategy to model their size distributions.

Since disruption by mechanical torques occurs at the lower end of the size distribution and disruption by radiative torques occurs at the high end, we can account for these disruption effects separately. As the size distributions of nanoparticles are poorly known, there is no strong conclusion whether this distribution should be a power law or log-normal. The power-law size distribution for nanoparticles was explored by Hensley & Draine (2017). In this work, we assume the size distribution of *original* nanoparticles to be log-normal following other studies (e.g., Draine & Lazarian 1998; Li & Draine 2001;

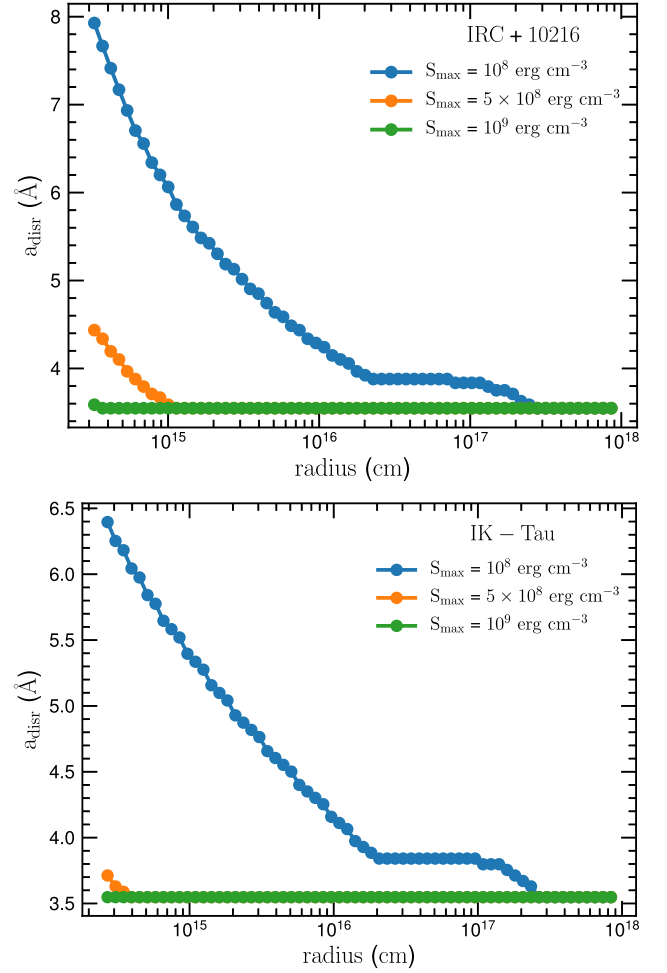


Figure 5. Minimum size below which PAHs are destroyed by rotational disruption vs. radius in the CSE around IRC +10216 (top panel) and IK Tau (bottom panel), assuming different material tensile strengths.

Hoang et al. 2016):

$$\frac{1}{n_H} \frac{dn_{\log\text{-norm}}}{da} = \frac{B}{a} \exp\left(-0.5 \left[\frac{\log(a/a_0)}{\sigma} \right]^2\right), \quad (23)$$

with $a_0 = 3\text{--}6 \text{ \AA}$, $\sigma = 0.3\text{--}0.6$ as the model parameters (see Table 1 in Li & Draine 2001), and the B constant determined by the a_0 , σ , and Y_X (fraction of total silicate ($X = \text{Si}$) or carbon ($X = \text{C}$) abundance contained in grains; see Equation 51 in Hoang & Tram 2019). The effect of rotational disruption by mechanical torques is then to increase the lower cutoff of the log-normal size distribution from $a_{min} = 3.5 \text{ \AA}$ to a_{cri} (see Figure 5).

To model the effect of rotational disruption by RATs, we assume that both *original* large grains and nanoparticles produced by disruption follow a power-law distribution with slope η :

$$\frac{1}{n_H} \frac{dn_{\text{powerlaw}}}{da} = A a^\eta, \quad (24)$$

where A is a normalization constant determined by the dust-to-gas-mass ratio ($M_{d/g}$) as

$$A = \frac{(4 + \eta) M_{d/g} m_{\text{gas}}}{\frac{4}{3} \pi \rho_{\text{bulk}} (a_{\text{max}}^{4+\eta} - a_{\text{min}}^{4+\eta})} \quad (25)$$

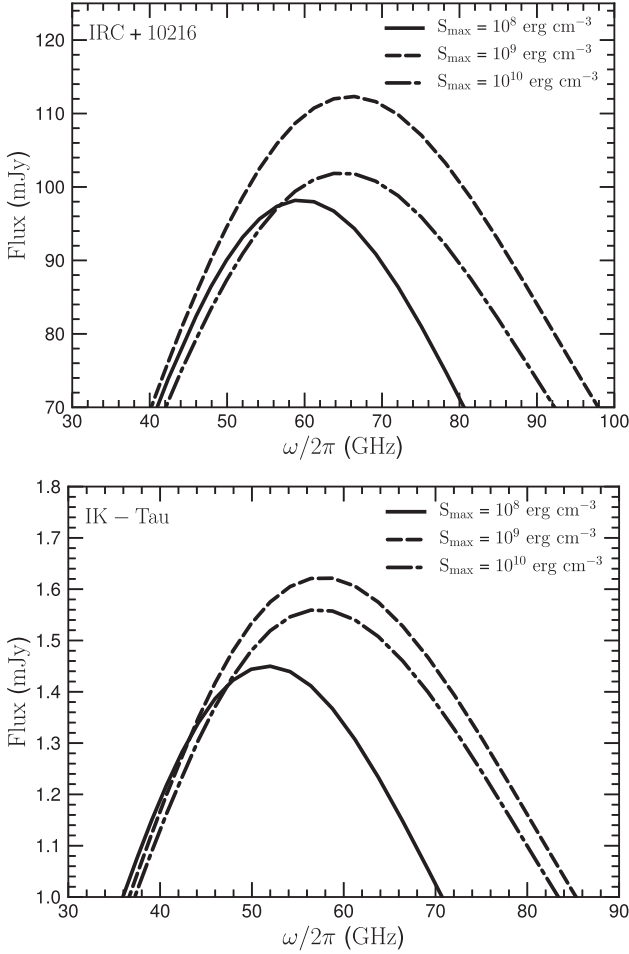


Figure 6. Emission flux from spinning nanoparticles in CSEs around a C-rich star (IRC+10216, top) and O-rich star (IK Tau, bottom). We adopt $M_{d/g} = 0.01$, $\eta = -3.5$, $\beta = 0.4D$, $Y_C \sim 0.05$ (Draine & Li 2007), and $Y_{Si} = 0.2$ (Hoang et al. 2016).

with a_{\max} being the upper constraint of grain size (Figure 3), and a_{\min} being the lower cutoff of grain sizes (Figure 5). Since Equation (25) is invalid for $\eta = -4$, the alternative expression of the constant A at this singularity is

$$\lim_{\eta \rightarrow -4} A = \frac{M_{d/g} m_{\text{gas}}}{\frac{4}{3} \pi \rho_{\text{bulk}} (\ln a_{\max} - \ln a_{\min})}. \quad (26)$$

For example, using a typical value of $M_{d/g} = 0.01$, $\eta = -3.5$, $a_{\min} = 50 \text{ \AA}$, and $a_{\max} = 0.25 \mu\text{m}$ we estimate $A \simeq 10^{-25.16} \text{ cm}^{-2.5}$ for carbonaceous grains (known as the MRN distribution, Mathis et al. 1977). With these parameters, the contribution of the power-law distribution is negligible compared to the log-normal size distribution (see, e.g., Draine & Lazarian 1998). In the presence of RATD, large grains are disrupted into smaller ones, so we can extend the power law to $a_{\min} = 3.5 \text{ \AA}$. Hence, the size distribution (Equation (24)) is modified such that the slope η becomes steeper, and the contribution of the power law becomes more important. Therefore, the net size distribution of nanoparticles is given by

$$\frac{dn}{da} = \frac{dn_{\log\text{-norm}}}{da} + \frac{dn_{\text{powerlaw}}}{da}. \quad (27)$$

Since the slope η is unknown, in the following we will consider several values for η . The dust-to-gas-mass ratio is likely to vary in practice, e.g., for IRC +10216: Agúndez & Cernicharo (2006) adopted $M_{d/g} = 0.002$, while Cernicharo et al. (2015) used $M_{d/g} = 0.004$; or for IK Tau: Decin et al. (2010) adopted $M_{d/g} = 0.02$, while Li et al. (2016) used $M_{d/g} = 0.01$.

5.2. Spinning Dust Emissivity

At any location in the CSE, the emissivity $j_\nu^a(\mu, T_{\text{rot}})$ from a spinning nanoparticle of size a is

$$j_\nu^a(\mu, T_{\text{rot}}) = \frac{1}{4\pi} P(\omega, \mu) 2\pi f_{\text{MW}}(\omega), \quad (28)$$

where $P(\omega, \mu)$ is the power emitted by a rotating dipole moment μ at angular velocity ω given by the Larmor formula,

$$P(\omega, \mu) = \frac{2}{3} \frac{\omega^4 \mu^2 \sin^2 \theta}{c^3}, \quad (29)$$

with θ being the angle between spin vector ω and moment vector μ . Assuming a uniform distribution of θ , then $\langle \sin^2 \theta \rangle = 2/3$. The dipole moment $\mu^2 \simeq 86.5(\beta/0.4D)^2 a^3 D^2$ for PAHs, and $\mu^2 \simeq 66.8(\beta/0.4D)^2 a^3 D^2$ for nanosilicates, in which β is the dipole per atom (Hoang et al. 2016). For PAHs, $\beta \simeq 0.4D$, while nanosilicates are expected to have a large dipole moment depending on selection of molecules (see Table 1 in Hoang et al. 2016). Therefore, we set β as a free parameter when calculating spinning emission for nanosilicates grains. The grain angular velocity f_{MW} can be appropriately described by a Maxwellian distribution in high-density conditions where collisional excitations dominate rotation of nanoparticles:

$$f_{\text{MW}}(\omega, T_{\text{rot}}) = \frac{4\pi}{(2\pi)^{3/2}} \frac{I^{3/2} \omega^2}{(k_B T_{\text{rot}})^{3/2}} \exp\left(-\frac{I\omega^2}{2k_B T_{\text{rot}}}\right). \quad (30)$$

The rotational emissivity per H nucleon is obtained by integrating over the grain-size distribution (see Hoang et al. 2011):

$$\frac{j_\nu(\mu, T_{\text{rot}})}{n_{\text{H}}} = \int_{a_{\min}}^{100 \text{ \AA}} j_\nu^a(\mu, T_{\text{rot}}) \frac{1}{n_{\text{H}}} \frac{dn}{da} da, \quad (31)$$

where dn/da is the size distribution for PAHs and nanosilicates (see Section 5.1).

5.3. Emission Spectrum of Spinning Dust

Assuming CSEs are spherically symmetric (see Figure 1 in Sahai & Chronopoulos 2010), which is justified in the intermediate and outer regions, i.e., $r > 5R_*$ (e.g., Agúndez & Cernicharo 2006; Decin et al. 2010), the spectral flux density of spinning dust is

$$F_\nu = \frac{1}{4\pi D^2} \int_{R_{\text{in}}}^{R_{\text{out}}} dr 4\pi r^2 n_{\text{H}}(r) \left[\frac{4\pi j_\nu(\mu, T_{\text{rot}})}{n_{\text{H}}} \right], \quad (32)$$

where D is the distance from the AGB star to the observer (see Table 1).

Figure 6 shows the emission spectrum of spinning PAHs in a C-rich star IRC +10216 (top panel) and nanosilicates in an O-rich star IK Tau (bottom panel) for different values of material strengths. For strong grains (e.g., $S_{\max} = 10^{10} \text{ erg cm}^{-3}$) for which rotational disruption does not occur, the spinning dust

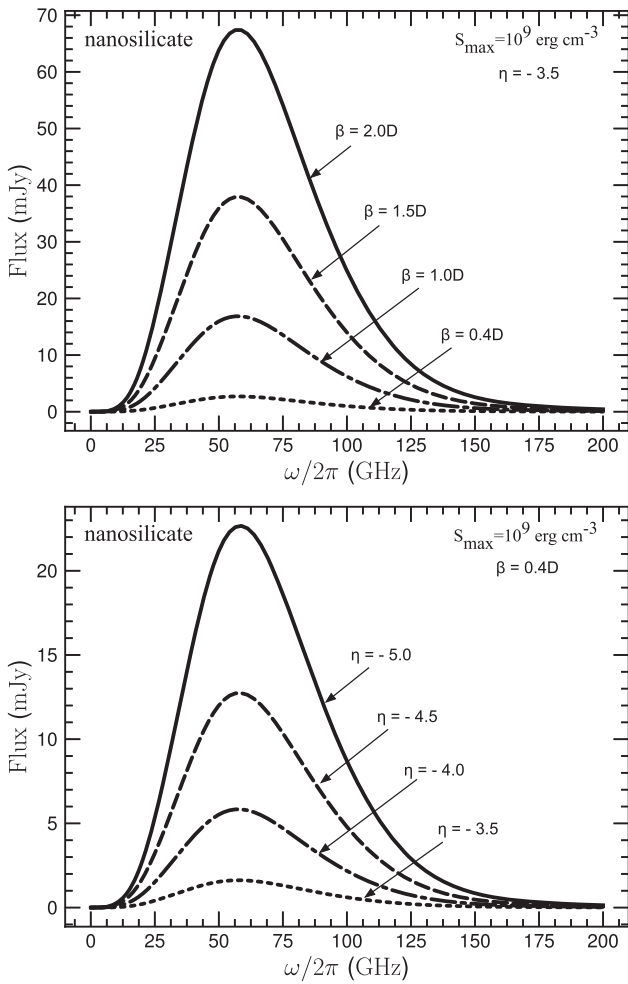


Figure 7. Modification of the emission spectrum from spinning nanosilicates around IK Tau: (top panel) varying the dipole per atom (β); and (bottom panel) varying the slope of the size distribution (η). Here the tensile strength $S_{\max} = 10^9 \text{ erg cm}^{-3}$ and $M_{d/g} = 0.01$ are assumed.

emissivity is strong and can peak at high frequencies (see the dashed lines). For weaker grains with rotational disruption, both the peak emissivity and peak frequency are reduced significantly because the smallest (and fastest-spinning) nanoparticles are destroyed into molecule clusters (see the dashed-dotted and solid lines).

The spectrum of spinning dust emission depends on both the dipole moment and the size distribution. The top panel of Figure 7 shows the increase of the emission flux from spinning nanosilicate grains with increasing dipole moment because the power emitted by a rotating dipole moment is proportional to β^2 . The peak frequency is insensitive to the β value because in the dense envelopes, electric dipole damping is subdominant compared to gas damping.

The bottom panel of Figure 7 shows the dependence of the spectrum on the slope of the size distribution, η . One can see that the peak emission flux tends to increase with increasing magnitude of slope, but the peak frequency does not change. Note that for the dust in the standard ISM, $\eta = -3.5$ (Mathis et al. 1977). For circumstellar dust, Dominik et al. (1989) estimated this index to be ~ -5 . The steeper size distribution might be explained by the enhancement of small particles owing to the disruption of large grains due to the RATD

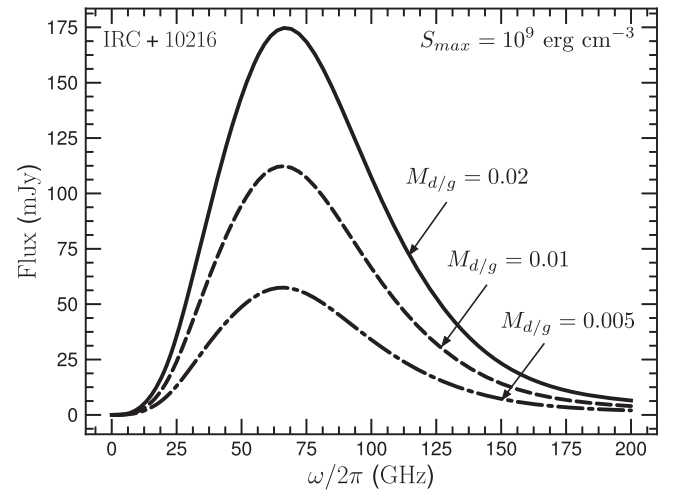


Figure 8. Effect of the dust-to-gas-mass ratio on the emission spectrum of spinning grains. We adopt $\beta = 0.4D$, $\eta = -3.5$.

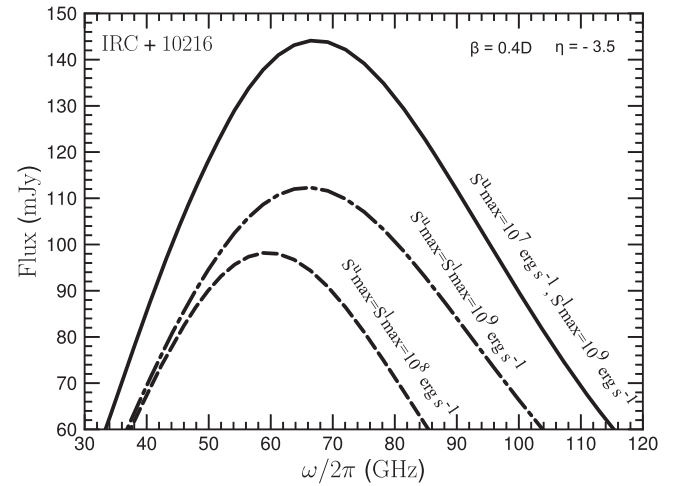


Figure 9. Effect of size-dependent tensile strength on the emission spectrum of spinning grains. We adopt $\beta = 0.4D$, $\eta = -3.5$, and $M_{d/g} = 0.01$.

mechanism. Therefore the constant A of the grain-size distribution increases for a steeper slope (see Equation (25)) and results in an increment of flux.

The dust-to-gas-mass ratio ($M_{d/g}$) also affects the spectrum of spinning dust emission. Figure 8 shows an example of the variation of a spinning spectrum over some values of $M_{d/g}$ calculated in the IRC +10216. The higher value of $M_{d/g}$ results in an increment of the flux since the constant A of the grain-size distribution is proportional to this quantity (see Equation (25)).

Above, we calculated the emission spectrum of spinning dust using the same value of S_{\max} for both large grains and small grains. In reality, the structure of small grains would be more compact, which should cause a higher value of S_{\max} than that for the large ones. Figure 9 shows the effect of the size-dependent tensile strength on the emission spectrum of spinning grains, in which we assume $S_{\max}^u = 10^7 \text{ erg cm}^{-3}$ for the upper constraint on grains sizes by RATD, and $S_{\max}^l = 10^9 \text{ erg cm}^{-3}$ for the lower constraint on those by mechanical torques. In this case, the emission flux has a higher amplitude (solid line) than the cases of constant $S_{\max} = 10^9 \text{ erg cm}^{-3}$. The underlying reason is the enhancement of nanoparticles because weaker large grains (i.e., low

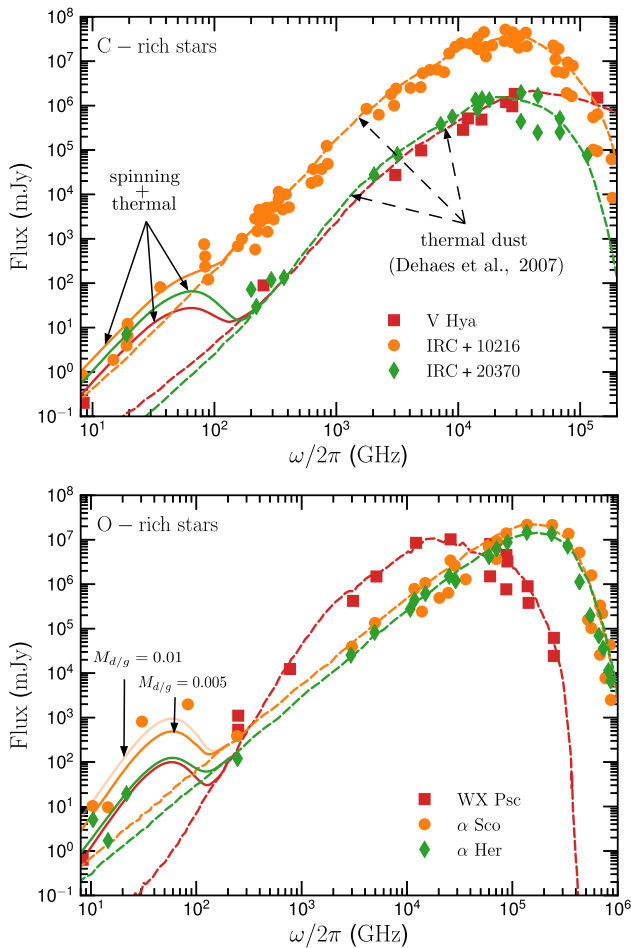


Figure 10. Comparison of spinning dust (solid lines, this work) and thermal dust (dashed lines, taken from Dehaes et al. 2007) models to radio observational data from the literature (filled symbols). The solid lines show that the spinning dust model can reproduce the CSEs of both C-rich (upper panel) and O-rich stars (lower panel). C-rich stars— $S_{\max} \geq 10^{10} \text{ erg cm}^{-3}$, $\beta = 0.4\text{D}$: $\eta = -3.7$ (IRC +10216), $\eta = -3.6$ (IRC +20370), and $\eta = -3.2$ (V Hya). O-rich stars— $S_{\max} \geq 10^9 \text{ erg cm}^{-3}$: $\beta = 2.3\text{D}$, $\eta = -5.0$ (α Sco); $\beta = 1.6\text{D}$, $\eta \sim -4.4$ (α Her); $\beta = 1.2\text{D}$, $\eta = -4.8$ (WX Psc). Note: The gas-to-gas-mass ratio is fixed as $M_{d/g} = 0.005$ as in Dehaes et al. (2007). The faint orange line likely indicates a higher dust-to-gas-mass ratio of $M_{d/g} \simeq 0.01$ in the case of α Sco.

values of S_{\max}) are more easily disrupted by RATD. Moreover, comparing to the case of the same S_{\max}^l (dashed-dotted line), the peak frequency does not change because the disruption effects of the smallest nanoparticles by mechanical torques are the same in both cases. So the peak frequency is much higher when comparing to the case of lower S_{\max}^l (dashed line) as shown in Figure 6.

6. Discussion

6.1. Rotational Disruption of Large Grains into Nanoparticles by Radiative Torques

We have studied the rotational disruption of large grains spun up by radiative torques using the theory developed by Hoang et al. (2019). As shown in Figure 3, owing to their extremely fast rotation, large grains are being disrupted into smaller fragments, including nanoparticles, which places a

constraint on the upper limit of the grain-size distribution in CSEs around AGB stars. The efficiency of rotational disruption is different for different locations along the radial trajectory of stellar winds (see Section 3). In addition, weak grains (i.e., tensile strength $S_{\max} \lesssim 10^9 \text{ erg cm}^{-3}$) are quite easily disrupted, while the disruption of stronger grains (i.e., tensile strength $S_{\max} \gtrsim 10^{10} \text{ erg cm}^{-3}$) is less efficient.

6.2. Removal of Nanoparticles Due to Rotational Disruption by Mechanical Torques

Due to stochastic collisions with neutral and ionized gas, plasma drag, and infrared emission, nanoparticles tend to rotate thermally/subthermally (Draine & Lazarian 1998; Hoang et al. 2010). Nevertheless, due to their small sizes (inertia moment), nanoparticles can rotate extremely fast, at rates higher than $10^{10} \text{ rad s}^{-1}$ (see Equation (22)). Subject to a supersonic gas flow induced by shocks (Hoang & Tram 2019; Tram & Hoang 2019) or radiation pressure as shown in this paper, nanoparticles can be spun up to suprathemal rotation, resulting in the disruption of the smallest nanoparticles into molecule clusters because the centrifugal stress exceeds the maximum tensile strength of nanoparticles. This mechanism places a constraint on the lower limit of the grain-size distribution. As shown in Figure 5, the disruption of nanoparticles is strongest near the central star and rapidly decreases moving outward. Moreover, nanoparticles of strong materials are hardly disrupted by mechanical torques in the AGB envelopes.

6.3. Can Spinning Dust Explain Excess Microwave Emission from AGB Envelopes?

The early detection of centimeter-wave observations toward the AGB stars, i.e., at 15 GHz (or 2 cm) and 20 GHz (or 1.5 cm) from IRC+10216 (Sahai et al. 1989), and at 8.4 GHz (or 3.57 cm) from four AGB stars from 21 samples (Knapp et al. 1995) cannot be explained by thermal dust emission. Recently, Dehaes et al. (2007) presented SED observations from a large sample of O-rich and C-rich AGB star envelopes and showed emission excess at centimeter wavelengths for many stars, including some post-AGB and supergiants with circumstellar shells. The authors divided them into two groups. Group I could be fitted successfully with thermal dust. Group II, on the other hand, is being fitted very well at optical and IR bands, but not being reproduced at centimeter-millimeter bands, including: IRC +10216, α Her, IRC +20370, WX Psc, α Sco, and V Hya (with central peak at $\lesssim 100$ GHz); and AFGL 1922, IRAS 15194-5115 (with a central peak at $\gtrsim 300$ GHz).

As shown in Section 5, the emission of spinning dust is strong and dominant over the thermal emission at the frequency $\lesssim 100$ GHz. Note that the overall purpose of this work is to demonstrate that spinning dust is one possible explanation for the AME detections in AGB envelopes, which would allow us to use our model calculated for IRC +10216 and IK Tau to fit the observational data of two C-rich and O-rich AGB stars, respectively. To fit the data, we vary three parameters S_{\max} , β , and η while fixing other physical parameters until we obtain the best-fit models. For the purpose of showing the whole SED, we combine the best models of the thermal dust emission provided by Dehaes et al. (2007), which were modeled by the DUSTY code (Ivezic et al. 1999), with $M_{d/g} = 0.005$. Figure 10 shows our best-fit models for observational data for three C-rich

(upper panel) and three O-rich (lower panel) stars given the corresponding set of parameters⁹ in the caption. Apparently, thermal dust and spinning dust are able to reproduce the millimeter–centimeter emission for both C-rich (top panel, Figure 10) and O-rich stars (bottom panel, Figure 10).

We note that some AGB stars such as AFGL 1922 and IRAS 15194-5115 exhibit submillimeter emission excess (i.e., at higher frequencies of $\gtrsim 250$ GHz). Furthermore, Dehaes et al. (2007) reported the variability at 1.2 mm ($\simeq 250$ GHz) for WX Psc and 1.1 mm ($\simeq 273$ GHz) for IRC +10216, and suggested that the variable molecular line emission might explain these large relative variations. However, such submillimeter excess cannot be reproduced by our standard spinning dust model presented here because spinning dust is known to be efficient at microwave frequencies. Very recently, Hoang & Tram (2019) and Tram & Hoang (2019) showed that spinning dust can be efficient at $\nu \gtrsim 200$ GHz in magnetized shocks where nanoparticles can be spun up to suprathermal rotation by supersonic neutral drift, provided that nanoparticles are strong enough to withstand disruption by centrifugal force. Indeed, termination shocks (or reversed shocks) could occur in CSEs when the stellar wind interacts with the surrounding ISM because the terminal velocity of the wind is supersonic (about $\sim 10\text{--}30$ km s⁻¹). Therefore, we propose that observing both the gas and the dust emission in the AGB envelopes should be crucial in order to better interpret the observable submillimeter emission excess because we could then have a better idea of where the termination shocks occur so that we could take the spinning dust emission from this shock into account.

Sahai et al. (2011) suggested submillimeter emission excess occurs by means of thermal emission from cold, very large grains (above 1 mm) post-AGB or pre-PN. However, how dust could grow to such large sizes in AGB envelopes is difficult to reconcile, because theoretical calculations show that dust released by AGB outflows is small grains (see, e.g., Jura 1994).

6.4. Implications for Future Observations

Further observations could help us distinguish the carrier of AME through comparing C-rich versus O-rich stars, because PAHs are formed in C-rich AGB stars, while silicates are formed in O-rich stars. Interferometers like ALMA and the VLA are capable of mapping the gas distribution around AGB stars and performing polarization observations to constrain the dust-grain properties in the shell (Khouri et al. 2018; Brunner et al. 2019). Such investigations are few in number, but they could help us understand dust nucleation and growth in wind-driven AGB stars.

Figure 10 in this paper presents spinning dust models fitted to available low-resolution radio observations of AGB stars. The low resolution, i.e., 1 data point (e.g., V Hya, WX Psc, IRC +20370), or a few data points (e.g., α Her), makes it difficult to distinguish whether the (se) excess point(s) resulted from the spinning dust or free-free or synchrotron or chromosphere emissions. High-resolution dust continuum observations from ALMA in bands 3, 4, and 5 at ~ 84 , 125, and 163 GHz, respectively, can improve constraints on fitted model parameters much better than available low-resolution observations, and the SED fitting can help resolve which mechanism (i.e.,

free-free, synchrotron, chromosphere, or spinning dust) is responsible for the AMEs in AGB envelopes. Additionally, carbon-rich stars such as IRC +10216 can be observed for different transitions of CO molecules (e.g., Cernicharo et al. 2015). The observations covering the ring structure will map the CO gas emission and hence the CSE of the star. Simultaneously, dust continuum observations at comparable resolutions will be useful to map the dust shell and hence spatially correlate it with gas emissions. Multiband observations of AGB stars from VLA with frequencies from 1 to 40 GHz may help with understanding the dust distribution when investigating the fluxes obtained in these frequencies and fitting SEDs. VLA plays an important role in covering regimes of frequencies less than 40 GHz (see Figure 10) at much higher resolutions than are used in the literature. Therefore, a combination of VLA and ALMA dust continuum observations in some of the bright AGB shells will help pin down the dust characteristics using our dust models.

VLA and ALMA also provide unique opportunities to map high-resolution dust continuum and line polarization. We can investigate whether the wind-swept shell regions of these AGB stars are polarized. The polarization measurements in the envelope of AGB stars will help with investigating dust-grain properties such as size and alignment efficiency.

6.5. Toward Constraining the Internal Structure of Dust Grains with Microwave Emission

By modeling the rotational disruption of grains and the resulting microwave emission from spinning dust, we find that microwave emission has a strong correlation with the tensile strength of grain materials. Both the peak flux and peak frequency tend to increase with increasing tensile strength (see Figure 7). This can be a powerful constraint on the internal structure of newly formed dust grains in AGB envelopes, which is still a mystery in dust astrophysics. Recently, Hoang (2019) suggested that the upper cutoff of the grain-size distribution in the ISM can be constrained by rotational disruption.

6.6. Model Uncertainties

In this section, we would stress the uncertainties and limitations of our model. First, we neglect the optical depth effect; thus we overestimate the radiation field strength in the envelope that would result in the RATD effect upon constraining the upper cutoff of grain size (see Figure 3), then change the grain-size distribution (see Equation (25)). Second, we assume the dust temperature varies as in Habing & Olofsson (2003; see Equation (3)), and derives from the radiative equilibrium, instead of solving the radiative transfer. This assumption is not correct for the nanoparticles responsible for spinning dust since they should be transiently heated, and their temperature should be higher. However, as spinning dust emission depends mostly on rotation rate, which is different from thermal dust emission, the effect of higher T_d is increasing thermal fluctuations of the principal grain axis with its angular momentum. The thermal fluctuation is ineffective at high values of dust temperature (Hoang et al. 2011). Third, we adopted the angular velocity that follows the Maxwellian distribution to calculate the spinning dust emissivity as Draine & Lazarian (1998) for the sake of simplicity. More generally, Ali-Haïmoud et al. (2009) used the Fokker–Planck equation to

⁹ The best-fit parameters are deduced from the model of spinning dust computed with the physical properties of IRC +10216 and IK Tau. Therefore, the exact parameters could be slightly different for other stars when using their physical properties adapted to them.

derive this distribution, and the predictions are not too much different from those of Draine & Lazarian (1998). Fourth, following Draine & Lazarian (1998) and Ali-Haimoud et al. (2009), our model disregarded the non-sphericity of grains and the anisotropy in the damping and excitation processes (i.e., ignore the magnetic field). Taking them into account, Hoang et al. (2010) indicated that the peak emissivity and the peak frequency of the spinning dust emission increase by a factor of a few. Fifth, since we do not know exactly the value of Y_{Si} in AGB envelopes, we fix the value of the $Y_{\text{Si}} = 20\%$ as an arbitrary parameter in this work within a reference that Li & Draine (2001) used to indicate that the upper limits for Y_{Si} in diffuse ISM for amorphous ultrasmall silicate grains is 30%. Moreover, the effect of Y_{Si} as shown in Figure 2 in Hoang et al. (2016) only causes variation of the emission flux. These uncertainties can modify the best-fit parameters in Figure 10, making it pertinent that the model is improved, and that specific models for each star are obtained.

Despite these uncertainties, we believe that our model still shows the principal characteristics of spinning dust, and that the spinning dust can be a good mechanism to explain the AME emissions in AGB envelopes.





7. Summary

We have studied rotational disruption of dust grains by radiative and mechanical torques in the AGB envelopes, performed detailed modeling of microwave emission from rapidly spinning nanoparticles, and applied the models to explain the observed excess microwave emission. The principle results are summarized as follows.

1. We model the rotational disruption of large grains by centrifugal stress induced by radiative torques from the central star. We find that large grains (e.g., $a > 0.1 \mu\text{m}$) made of weak materials (tensile strength $S_{\text{max}} \lesssim 10^9 \text{ erg cm}^{-3}$) can be disrupted into nanoparticles within a radius of 10^{16} cm from the star.
2. We also study the disruption of nanoparticles by centrifugal stress due to stochastic collisions of grains with supersonic gas flow driven by radiation pressure and find that the smallest nanoparticles of weak materials located close to the star can be destroyed.
3. We model microwave emission from spinning PAHs and silicate nanoparticles in C-rich and O-rich envelopes. We find that due to the radial dependence of the gas temperature, the spinning dust emits over a wide range of microwave frequencies.
4. We found that microwave emission from either spinning PAHs or spinning nanosilicates can dominate over thermal dust at frequencies $\nu < 100 \text{ GHz}$ in the AGB envelopes.
5. By fitting the spinning dust to observed data from millimeter to centimeter wavelengths, we find that AME observed in AGB envelopes can be successfully reproduced by microwave emission from carbonaceous or silicate nanoparticles.
6. Thanks to the correlation of spinning dust flux with the grain tensile strength, we suggest that the internal structure of newly formed dust in AGB envelopes can be probed with microwave emission observations.

We thank the anonymous referee for helpful comments that improved the impact and the presentation of this paper. T.L.N. is funded by the SOFIA postdoctoral fellowship. H.T. acknowledges the financial support from the Basic Science Research Program through the National Research Foundation of Korea (NRF) funded by the Ministry of Education (2017R1D1A1B03035359). A.S. acknowledges the financial support from the NSF through grant AST-1715876.

ORCID iDs

Le Ngoc Tram  <https://orcid.org/0000-0002-6488-8227>
 Thiem Hoang  <https://orcid.org/0000-0003-2017-0982>
 Archana Soam  <https://orcid.org/0000-0002-6386-2906>
 William T. Reach  <https://orcid.org/0000-0001-8362-4094>

References

- Agúndez, M., & Cernicharo, J. 2006, *ApJ*, **650**, 374
 Akimkin, V., Zhukovska, S., Wiebe, D., et al. 2013, *ApJ*, **766**, 8
 Ali-Haimoud, Y., Hirata, C. M., & Dickinson, C. 2009, *MNRAS*, **395**, 1055
 Allamandola, L. J., Tielens, A. G. G. M., & Barker, J. R. 1985, *ApJL*, **290**, L25
 Brunner, M., Mecina, M., Maercker, M., et al. 2019, *A&A*, **621**, A50
 Burke, J. R., & Silk, J. 1974, *ApJ*, **190**, 1
 Castellanos, P., Casassus, S., Dickinson, C., et al. 2011, *MNRAS*, **411**, 1137
 Cernicharo, J., Guélin, M., & Kahane, C. 2000, *A&AS*, **142**, 181
 Cernicharo, J., Marcelino, N., Agúndez, M., & Guélin, M. 2015, *A&A*, **575**, A91
 Cherchneff, I. 2011, in EAS Publications Series 46, PAHs and the Universe: A Symp. to Celebrate the 25th Anniversary of the PAH Hypothesis, 46 (Les Ulis: EDP Sciences), 177
 Cox, N. L. J., Kerschbaum, F., van Marle, A.-J., et al. 2012, *A&A*, **537**, A35
 Crosas, M., & Menten, K. M. 1997, *ApJ*, **483**, 913
 De Beck, E., Decin, L., de Koter, A., et al. 2010, *A&A*, **523**, A18
 Decin, L., De Beck, E., Brünken, S., et al. 2010, *A&A*, **516**, A69
 Dehaes, S., Groenewegen, M. A. T., Decin, L., et al. 2007, *MNRAS*, **377**, 931
 Dominik, C., Gail, H. P., & Sedlmayr, E. 1989, *A&A*, **223**, 227
 Draine, B. T., & Lazarian, A. 1998, *ApJ*, **508**, 157
 Draine, B. T., & Li, A. 2007, *ApJ*, **657**, 810
 Draine, B. T., & Salpeter, E. E. 1979, *ApJ*, **231**, 77
 Draine, B. T., & Weingartner, J. C. 1996, *ApJ*, **470**, 551
 Fleming, T., & Stone, J. M. 2003, *ApJ*, **585**, 908
 Gilman, R. C. 1972, *ApJ*, **178**, 423
 Glassgold, A. E., & Huggins, P. J. 1983, *MNRAS*, **203**, 517
 Guhathakurta, P., & Draine, B. T. 1989, *ApJ*, **345**, 230
 Habing, H. J., & Olofsson, H. 2003, *Asymptotic Giant Branch Stars* (Berlin: Springer)
 Hensley, B. S., & Draine, B. T. 2017, *ApJ*, **836**, 179
 Herranen, J., Lazarian, A., & Hoang, T. 2019, *ApJ*, **878**, 96
 Hoang, T. 2017, *ApJ*, **847**, 77
 Hoang, T. 2019, *ApJ*, **876**, 13
 Hoang, T., Draine, B. T., & Lazarian, A. 2010, *ApJ*, **715**, 1462
 Hoang, T., & Lazarian, A. 2008, *MNRAS*, **388**, 117
 Hoang, T., & Lazarian, A. 2016, *ApJ*, **821**, 91
 Hoang, T., Lazarian, A., & Draine, B. T. 2011, *ApJ*, **741**, 87
 Hoang, T., & Tram, L. N. 2019, *ApJ*, **877**, 36
 Hoang, T., Tram, L. N., Lee, H., et al. 2019, *NatAs*, **3**, 766
 Hoang, T., Vinh, N. A., & Quynh Lan, N. 2016, *ApJ*, **824**, 18
 Hoefner, S., & Dorfi, E. A. 1997, *A&A*, **319**, 648
 Ivezic, Z., Nenkova, M., & Elitzur, M. 1999, DUSTY: Radiation transport in a dusty environment, Astrophysics Source Code Library, ascl:9911.001
 Jaeger, C., Molster, F. J., Dorschner, J., et al. 1998, *A&A*, **339**, 904
 Jones, R. V., & Spitzer, L. J. 1967, *ApJ*, **147**, 943
 Jura, M. 1994, *ApJ*, **434**, 713
 Justtanont, K., Khouri, T., Maercker, M., et al. 2012, *A&A*, **537**, A144
 Khouri, T., Vlemmings, W. H. T., Olofsson, H., et al. 2018, *A&A*, **620**, A75
 Knapp, G. R., Bowers, P. F., Young, K., & Phillips, T. G. 1995, *ApJ*, **455**, 293
 Knapp, G. R., Young, K., Lee, E., & Jorissen, A. 1998, *ApJS*, **117**, 209
 Krueger, D., Gauger, A., & Sedlmayr, E. 1994, *A&A*, **290**, 573
 Kwan, J., & Linke, R. A. 1982, *ApJ*, **254**, 587
 Kwok, S. 2004, *Natur*, **430**, 985
 Lamers, H. J. G. L. M., & Cassinelli, J. P. 1999, *Introduction to Stellar Winds* (Cambridge: Cambridge Univ. Press)

- Lazarian, A., & Hoang, T. 2007, *MNRAS*, **378**, 910
- Leger, A., & Puget, J.-L. 1984, *A&A*, **137**, L5
- Li, A., & Draine, B. T. 2001, *ApJL*, **550**, L213
- Li, X., Millar, T. J., Heays, A. N., et al. 2016, *A&A*, **588**, A4
- Maercker, M., Danilovich, T., Olofsson, H., et al. 2016, *A&A*, **591**, A44
- Mamon, G. A., Glassgold, A. E., & Huggins, P. J. 1988, *ApJ*, **328**, 797
- Mathis, J. S., Mezger, P. G., & Panagia, N. 1983, *A&A*, **500**, 259
- Mathis, J. S., Rumpl, W., & Nordsieck, K. H. 1977, *ApJ*, **217**, 425
- Mathis, J. S., & Whiffen, G. 1989, *ApJ*, **341**, 808
- Matthews, L. D., Gérard, E., & Le Bertre, T. 2015, *MNRAS*, **449**, 220
- Menten, K. M., Reid, M. J., Kamiński, T., & Claussen, M. J. 2012, *A&A*, **543**, A73
- Menten, K. M., Reid, M. J., Krügel, E., Claussen, M. J., & Sahai, R. 2006, *A&A*, **453**, 301
- Millar, T. J., Herbst, E., & Bettens, R. P. A. 2000, *MNRAS*, **316**, 195
- Olofsson, H., Maercker, M., Eriksson, K., Gustafsson, B., & Schöier, F. 2010, *A&A*, **515**, A27
- Ramstedt, S., Maercker, M., Olofsson, G., Olofsson, H., & Schöier, F. L. 2011, *A&A*, **531**, A148
- Roberge, W. G., Hanany, S., & Messinger, D. W. 1995, *ApJ*, **453**, 238
- Sahai, R., & Chronopoulos, C. K. 2010, *ApJL*, **711**, L53
- Sahai, R., Claussen, M. J., & Masson, C. R. 1989, *A&A*, **220**, 92
- Sahai, R., Claussen, M. J., Schnee, S., Morris, M. R., & Sánchez Contreras, C. 2011, *ApJL*, **739**, L3
- Smith, J.-D. T., Draine, B. T., Dale, D. A., et al. 2007, *ApJ*, **656**, 770
- Tenenbaum, E. D., Dodd, J. L., Milam, S. N., Woolf, N. J., & Ziurys, L. M. 2010, *ApJL*, **720**, L102
- Tielens, A. G. G. M. 1983, *ApJ*, **271**, 702
- Tielens, A. G. G. M. 2008, *ARA&A*, **46**, 289
- Tram, L. N., & Hoang, T. 2019, *ApJ*, **886**, 44
- Tram, L. N., Lesaffre, P., Cabrit, S., & Nhung, P. T. 2018, arXiv:1808.01439
- Willson, L. A. 2000, *ARA&A*, **38**, 227
- Winters, J. M., Dominik, C., & Sedlmayr, E. 1994, *A&A*, **288**, 255